Experimental and Theoretical Analysis of the Combustion Efficiency and the Heat Loads on a N_2O/C_2H_4 Green Propellant Combustion Chamber

Lukas Werling [†]*, Till Hörger, Helmut Ciezki and Stefan Schlechtriem*
German Aerospace Center (DLR)
Im Langen Grund, 74239 Hardthausen, Germany
Lukas.Werling@dlr.de · Till.Hoerger@dlr.de · Helmut.Ciezki@dlr.de · Stefan.Schlechtriem@dlr.de
[†]Corresponding author

Abstract

Currently several green propellants as substitute for the highly toxic hydrazine are under investigation. A possible alternative are so called nitrous oxide fuel blends. This paper presents the results of combustion tests conducted with a premixed monopropellant consisting of N_2O and C_2H_4. In four test series the influence of the mixture ratio, the chamber pressure, the chamber length and the mass flux on the combustion efficiency and on the heat flux is analyzed and discussed. Furthermore four empirical Nusselt correlations derived by Bartz, Cinjarew, Dittus-Boelter and Gnielinski are compared to the experimental results and finally modified to improve their accuracy.

1. Introduction

The global quest for green propellant alternatives to the highly toxic hydrazine (N_2H_4) is still ongoing. Different alternatives for monopropellant hydrazine with different degrees of maturity are currently under investigation. Among those are hydrogen peroxide (H_2O_2), Ammonium dinitramide (ADN) based propellants as LMP-103S, HAN (hydroxylammonium nitrate) based propellants as AFM-315E, water propulsion systems and nitrous oxide fuel blends. All mentioned propellants or systems come along with several advantages or disadvantages compared to conventional hydrazine:

High concentrated hydrogen peroxide (H_2O_2) is non-toxic, has a high density, cold start capable catalysts are available and can be used as oxidizer in bipropellant systems.[9, 18, 27] Despite those advantages the specific impulse of H_2O_2 is not very high (I_{sp} max. 185 s), long term storability might be tricky and material compatibility with many currently used materials is a big issue.[10, 17, 19]

ADN based propellants deliver a high specific impulse (LMP-103S $\approx$ 253 s,[33] FLP-106 $\approx$ 260 s[15]), offer a high density and a low toxicity.[3–5, 12] Drawbacks regarding ADN based propellants are that catalysts for cold start operations are not available,[31, 43] so preheating is required, upscaling of thrusters seems to be a difficult challenge and high temperature alloys are needed to handle the combustion temperatures ($\approx$ 1903 K[31]).

HAN based propellants (AFM-315E or SHP 163) might offer a similar or even higher performance than ADN based propellants ($I_{sp} \approx$ 248 s[28, 35] or 276 s[2] respectively). Those propellants show a high density ($\approx$ 1400 kg/m^3)[2] and a low toxicity. On the other hand HAN based propellants tend to be explosive,[22] high temperature chamber materials need to be deployed and catalysts may be damaged due to the high combustion temperatures. A test flight (NASA Green Propellant Infusion Mission - GPIM) was postponed several times[34] and is now scheduled for June 2019. Currently a 1 N thruster is intended to fly on the GPIM, while a 22 N thruster is still under development.[28]

Furthermore the so called "water electrolysis propulsion" is another promising candidate regarding green orbital propulsion.[17, 20, 21] Those propulsion systems consist of a water tank, an electrolyzer, a hydrogen and an oxygen buffer tank, and the thruster. The satellite is fueled with water and during the operation in orbit the water is split into hydrogen and oxygen via electrolysis. The gaseous H_2 and O_2 is then stored in separate tanks and fed to a thruster equipped with a catalyst to propel the spacecraft. This propulsion system can achieve a high specific impulse ($I_{sp} >$ 300 s), the propellant is cheap, completely green and non-toxic. One the opposite the propulsion system is quite complex and thus prone to errors, the high combustion temperatures need to be addressed with a cooling system and the thrust level and thrust duration is limited by the tank and electrolyzer sizes.

ANALYSIS OF COMBUSTION EFFICIENCY AND HEAT LOADS AN A N$_2$O/C$_2$H$_4$ COMBUSTOR

Another class of green propellants are mixtures of nitrous oxide and a fuel, which often are referred to as nitrous oxide fuel blends.[29, 30, 37, 38, 40, 41] Those propellants are stored in premixed, liquid state and comprise hydrocarbons or alcohols as fuels and nitrous oxide as oxidizer. Advantages of nitrous oxide fuels blends are their high I$_{sp}$ (> 300 s), the cheap and non-toxic components as well as the possibility to realize a self-pressurized propulsion system. Drawbacks are the high combustion temperatures (up to $\approx$ 3400 K) and the hazards connected to flame flashback and possible explosion of the propellant mixture.[39] Since 2014 DLR's Institute of Space Propulsion investigates a nitrous oxide fuel blend, consisting of nitrous oxide (N$_2$O) and ethene (C$_2$H$_4$), which is called "HyNOx" (Hydrocarbons and Nitrous Oxide). Due to the above mentioned challenges, DLR's research was focused on how to avoid flame flashback and on the development of suitable flashback arresters[39, 40] for a gaseous N$_2$O/C$_2$H$_4$ propellant. A specific ignition and flashback setup was used to evaluate the quenching capability of different flashback arresters.

In parallel to those quenching experiments, the flame arresters were used in an experimental rocket combustion chamber to evaluate their flame quenching performance with regard to the later application. Several hot gas test campaigns with a gaseous, premixed N$_2$O/C$_2$H$_4$ mixture were conducted.[38, 41] During this campaigns the operation ranges and the operation limits of the flashback arresters were determined. Besides the examination of the flashback arresters, a first analysis of the propellant performance, occurring heat loads and the needed combustion chamber size (L^*) was conducted.[32, 37, 38] Due to the use of a capacitively cooled combustion chamber and the premixed, gaseous state of the propellant, the combustion efficiency is strongly connected to the heat loss to the chamber walls. In addition the heat fluxes to the chamber walls need to be evaluated, to be able to design a regenerative cooling system for a future thruster. By knowing the heat loads a appropriate cooling channel design for the thruster can be chosen and overheating of the material and structure is avoided.

To generate a valid dataset of the occurring heat loads, as well as to determine the characteristic exhaust velocity c^* and the combustion efficiency η_{c^*} a test campaign with variation of the mixture ratio, the chamber pressure, the chamber length and the mass flux was conducted. The overall heat flux to the chamber walls was derived by using the temperature rise in the chamber walls during the combustion tests. The resulting heat flux data were subsequently compared to analytical correlations. The analytical Nusselt correlations used for the comparison are the commonly used Bartz equation,[8] the Dittus-Boelter correlation,[24] a correlation derived by Cinjarew[13, 26] and one obtained by Gnielinski.[14] This paper summarizes the theoretical and experimental results regarding the propellant performance (c^* and η_{c*}), furthermore the predictions of the Nusselt correlations are presented and compared to the experimental values. The analysis concludes with a modified and optimized Nusselt correlation for the used propellant and combustion chamber.

2. Theoretical Background

2.1 Characteristic Exhaust Velocity c^* and Combustion Efficiency η_{c*}

The characteristic exhaust velocity c^* is a commonly used parameter to evaluate the performance of a rocket propellant. By comparing the experimentally determined c^* (c^*_{exp}) to the theoretical c^* (c^*_{theo}), the c^* efficiency or combustion efficiency (η_{c^*}) can be derived. Reduced c^*_{exp} and a corresponding reduced η_{c^*} show losses in the combustion chamber caused by heat fluxes, chemical non-equilibrium, non-ideal mixing, mixture ratio variations, incomplete combustion, boundary layers or due to non-uniformities of the overall flow field. To determine the overall system performance and to take also nozzle effects into account, the specific impulse I_{sp} is a widely used parameter.[36]

The characteristic velocity c^* is depending on the injector design, the propellant itself, the mixture ratio, the chamber pressure and the combustion chamber size.[36] Compared to the specific impulse I_{sp}, c^* is independent on the nozzle shape and expansion ratio. So by means of c^* different propellant and injector combinations as well as combustion chamber designs can be compared to each other. To derive the experimental c^* from test data, equation (1) is used:

$$c^*_{exp} = \frac{p_c \cdot A_{th}}{\dot{m}} \tag{1}$$

Here p_c is the stagnation pressure in the combustor, $\dot{m}$ symbolizes the propellant mass flow and A_{th} the nozzle throat area. For the later analysis, the experimentally obtained c^*_{exp} is divided by the theoretical c^*_{theo} determined via NASA CEA code[16] to obtain the combustion efficiency η_{c^*}:

$$\eta_{c^*} = \frac{c^*_{exp}}{c^*_{theo}} \tag{2}$$

The characteristic combustion chamber length L^* is a further commonly used design parameter for rocket combustion chambers. L^* is defined as the chamber volume V_{cc} divided by the nozzle throat area A_{th}:

2

$$L^* = \frac{V_{cc}}{A_{th}} \tag{3}$$

if the cross-sectional area of the combustion chamber A_{cc} is constant and the volume of the injector plate and the volume of the converging part of the nozzle is neglected, the length of the chamber L_{cc}, L^* can be written as:

$$L^* \approx \frac{L_{cc} \cdot A_{cc}}{A_{th}} \tag{4}$$

The optimum L^* for a given chamber geometry, injection system and propellant combination is achieved, if c^* and the corresponding combustion efficiency η_{c*} reach a maximum. On the one hand, if L^* is too short, the propellant might not burn completely and the efficiency is reduced. On the other hand, if the chamber is too long and not equipped with a regenerative cooling system, heat losses to the chamber walls and to the environment will diminish the combustion efficiency.

2.2 Heat Fluxes/Heat Loads in Rocket Combustion Chambers

The combustion temperature of nitrous oxide and ethene can get as high as $3300K$. In general, the temperature of the combustion chamber wall is significantly lower than the combustion temperature. Therefore a heat flux from the hot gas into the chamber wall appears. To avoid melting or overheating of the chamber walls, the heat flux applied to the walls is of great interest for the design of a combustion chamber. Furthermore the precise knowledge of the occurring heat loads is crucial to design an appropriate regenerative cooling system. One option to determine the heat flux to the combustor is to employ CFD simulations of the combustion and the flow field inside the chamber. Another less costly option is to calculate the heat flux by using a so called Nusselt correlation. The Nusselt number Nu is defined as follows:[1,6]

$$Nu = \frac{\alpha l}{\lambda} \tag{5}$$

With α being the convective heat transfer coefficient, l a characteristic length scale of the flow and λ the thermal conductivity. Concerning the average Nusselt number Nu_m for a given surface area, the rate of heat flow $\dot{Q}$ applied to this area can be calculated via equation (6):

$$\dot{Q} = \frac{Nu_m \lambda}{l} \left(T_{ref} - T_{wall} \right) A_{ref} \tag{6}$$

While A_{ref} denotes the reference surface area, T_{wall} the wall temperature and T_{ref} the reference temperature of the fluid. Furthermore the heat flux $\dot{q}$ is defined as:

$$\dot{q} = \frac{\dot{Q}}{A_{ref}} \tag{7}$$

For the analysis of the later described combustion test, it was assumed that the convective heat transfer from the combustion process will result in a heating of the combustion chamber walls.

$$\dot{q} = \dot{q}_{wall} \tag{8}$$

Thus the mass of the chamber segments m_{seg}, the heat capacity c_p, the chamber segments surface area A_{seg}, the test duration Δt and the temperature rise in the chamber walls ΔT was taken into account to calculate the heat flux $\dot{q}$ to the chamber walls:

$$\dot{q}_{wall} = \frac{m_{seg} \cdot c_p \cdot \Delta T}{\Delta t \cdot A_{seg}} \tag{9}$$

Regarding the analytical description of the heat flux (equation (6)), the average Nusselt number is only a function of the dimensionless variables Reynolds number Re, Prandtl number Pr, Grashof number Gr and Eckert number Ec.[6]

$$Nu_m = f(Re, Pr, Gr, Ec,) \tag{10}$$

For cases in which no free convection occurs and the Mach numbers are low, Ma, Gr and Ec can be neglected.[1] For this cases the Nussel number is only a function of the Reynolds Re and Prandtl Pr number:

$$Re = \frac{\rho \cdot v \cdot l}{\mu} \tag{11}$$

ANALYSIS OF COMBUSTION EFFICIENCY AND HEAT LOADS AN A N_2O/C_2H_4 COMBUSTOR

$$Pr = \frac{\mu \cdot c_p}{\lambda} \tag{12}$$

Here ρ is the density, v the flow velocity, l a characteristic length scale, as for example the hydraulic diameter d_h, μ the dynamic viscosity, c_p the specific heat at constant pressure and λ the heat conductivity of the fluid. During the last decades several semi-empirical correlations have been established to determine the value of the Nusselt number for different flow conditions and applications. For a fully developed turbulent pipe flow the Dittus-Boelter equation (13) gives a first estimation of the Nusselt number:[24]

$$Nu_{m,DB} = 0.023Re^{0.8}Pr^n \tag{13}$$

With the following limitations:

$$10000 \leq Re$$
$$0.7 \leq Pr \leq 160$$
$$10 \leq l_{pipe}/d \leq \infty$$

Here d is the diameter and l the length of the pipe. The exponent n depends on corresponding heating or cooling process. So for heating of the wall by the fluid $n = 0.3$, for cooling of the wall by the flow $n = 0.4$. The thermo-physical properties which are needed to calculate Re and Pr have to be determined at a reference temperature. Regarding the original form of the Dittus-Boelter equation the reference temperature $T_{ref,DB}$ for a pipe flow is the mean value of the fluids inlet and T_{in} and outlet temperature T_{out} :

$$T_{ref,DB} = \frac{T_{in} + T_{out}}{2} \tag{14}$$

Especially for rocket combustors Cinjarew proposed the following equation:[25,26]

$$Nu_{m,Ci} = 0.0162 \left(Re \cdot Pr \right)^{0.82} \left(\frac{T_{Stag}}{T_{wall}} \right)^{0.35} \tag{15}$$

with the stagnation temperature T_{stag}. While T_{stag} is defined as:

$$T_{stag} = T_{stat} + r_c \cdot (T_c \cdot \eta_{c^*}^2 - T_{stat}) \tag{16}$$

Here T_{stat} is the static temperature of the fluid, T_c the adiabatic combustion temperature, η_{c^*} the combustion efficiency and r_c the recovery factor. The recovery factor is an empirical value and usually ranges from 0.7 and 0.9.[25] Furthermore, the static temperature T_{stat} is defined as:

$$T_{stat} = \frac{T_c}{1 + \frac{\kappa-1}{2} Ma^2} \tag{17}$$

With the Mach Number Ma and the heat capacity ratio κ. According to the initial equation, the fluid properties for the calculation of the Prandtl and Reynolds number have to be determine at the wall temperature T_{wall}. In contrast Kirchberger[25] gained a better agreement with experimental data by using the mean value of the adiabatic combustion temperature T_c and the wall temperature T_{wall} for calculation of the viscosity, thermal conductivity and the heat capacity:

$$T_{mean} = \frac{T_c + T_{wall}}{2} \tag{18}$$

A more general equation is given by Gnielinski:[1,14]

$$Nu_{m,Gn} = \frac{\frac{\xi}{8}(Re - 1000) \cdot Pr}{1 + 12.7 \cdot \sqrt{\frac{\xi}{8}} \left(Pr^{\frac{2}{3}} - 1 \right)} \left[1 + \left(\frac{d_h}{l_{pipe}} \right)^{\frac{2}{3}} \right] \tag{19}$$

Gnielinskis correlation additionally takes the hydraulic diameter d_h and the length l_{pipe} of the pipe into account. Additionally ξ is defined as:

$$\xi = (1.82 log(Re) - 1.64)^{-2} \tag{20}$$

The correlation derived by Gnielinski is valid for a Reynolds number Re, Prandlt number Pr and length l to diameter d_h ratio of:

$$10^4 \leq Re \leq 10^6$$
$$0, 1 \leq Pr \leq 1000$$
$$l_{pipe}/d_h \geq 1$$

The fluid properties for the Gnielinski equation must also be evaluated at the mean temperature T_{mean} according to equation (18).

For rocket engines and especially rocket nozzles Bartz[8] derived a correlation under consideration of the thermal and velocity boundary layer:

$$Nu_{m,Ba} = 0.026 \cdot Re^{0.8} \cdot Pr^{0.4} \left(\frac{d_{th}}{r_{BK}} \right)^{0.1} \cdot \sigma_B \tag{21}$$

while σ_B is defined as:

$$\sigma_B = \left[0.5 \cdot \frac{T_{wall}}{T_{Stag}} \left(1 + \frac{\kappa - 1}{2} Ma^2 \right) + 0.5 \right]^{-0.68} \left[1 + \frac{\kappa - 1}{2} Ma^2 \right]^{-0.12} \tag{22}$$

d_{th} is the nozzle throat diameter, r_{BK} is the radius of the combustion chamber and κ the ratio of the specific heats. Bartz proposed to evaluate c_p and Pr for the conditions at the stagnation temperature T_{stag}, while and μ and ρ should be evaluated at the mean temperature T_{mean}.[7]

3. Experimental Setup and Test Conduction

In the following section the test bench layout, the piping and instrumentation diagram and the used combustor are described. Furthermore the test procedure is explained. The combustion tests were conducted at DLRs M11 test facility.[11,42]
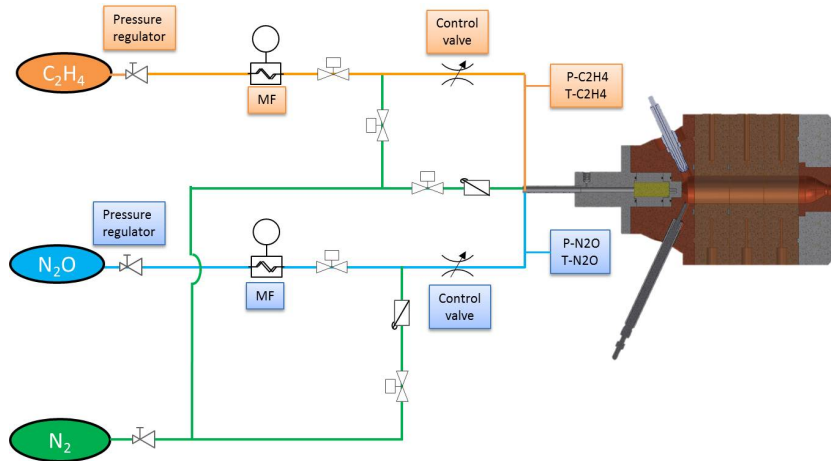
3.1 Test Bench Layout and P&ID

Figure 1: Simplified piping and instrumentation diagram of the test setup

Figure 1 shows a simplified piping and instrumentation diagram (P&ID) of the test setup. The left hand side of the figure shows the gas supply, the used C_2H_4 had a purity of 3.0, while the N_2O was garde 5.0. Downstream the gas bottles in each feeding line a pressure regulator is mounted, it is used to adjust the supply pressure and mass flow to the combustion chamber. The nitrous oxide and ethene feeding lines are each equipped with a Coriolis mass flow meter (Rheonik RHM015 and RHM04), a 2-2 way valve and a control valve to adjust the mixture ratio and mass flow. Upstream the combustor, the nitrous oxide and ethene feeding lines are connected at a pipe crossing and after a mixing section the oxidizer and fuel are injected in premixed state in the combustion chamber.

The supply pressure and the feeding temperature upstream the tube crossing and the injector are measured via pressure transducers (P-C2H4, P-N2O) and thermocouples (T-C2H4, T-N2O). The data acquisition rate for the pressure sensors is 5 kHz while the data of the thermocouples and the mass flow are recorded with 100 Hz and 10 Hz, respectively.

ANALYSIS OF COMBUSTION EFFICIENCY AND HEAT LOADS AN A N_2O/C_2H_4 COMBUSTOR
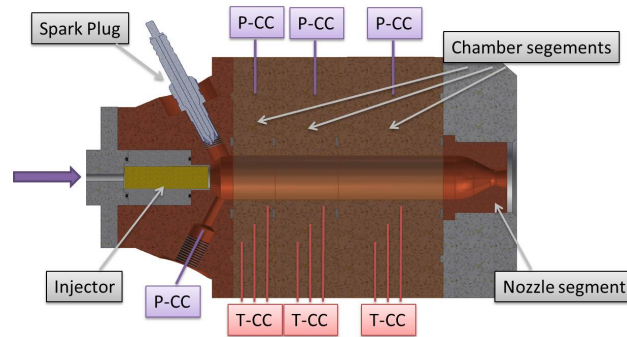
3.2 Combustion Chamber

Figure 2: Sectional view of the combustion chamber

Figure 2 show a sectional view of the combustion chamber. The gaseous propellant mixture enters the combustor at the left hand side through the feeding line and the injector. To ignite the mixture, a spark plug is used. Opposite to the spark plug at the the injector faceplate a pressure transducers is mounted. The influence of the chamber length (L^*) can be investigated by using different numbers of segments, which additionally vary in length.

Each chamber segment is equipped with three thermocouples in 3, 8 and 13 mm radial distance to the inner chamber wall and an additional pressure sensor. The segments and the nozzle as well as the injector fitting are made of CuCr1Zr. Convergent-divergent nozzle with throat diameters ranging from 5 mm to 9 mm are available, while the inner diameter of the combustion chamber is 24 mm. By combining the different segments and nozzles a wide variation of the characteristic combustion chamber length L^* is achieved. The chamber has no active cooling system, so the heat generated by the combustion results in a temperature rise of the chamber segments, faceplate and nozzle.
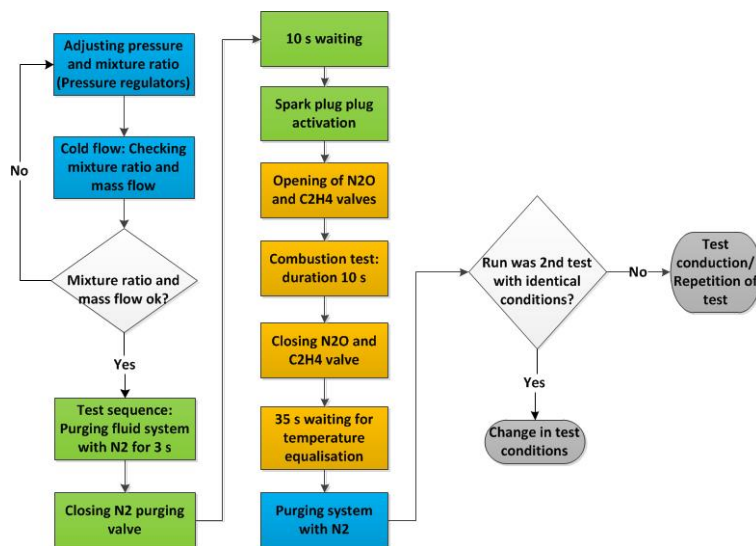
3.3 Test Conduction and Sequence

Figure 3: Schematic of the test sequence

The test procedure is visualized in Figure 3. Prior to the test sequences, the combustion chamber and the whole setup were leak tested. At the beginning of a test sequence, the mixture ratio and pressure were adjusted by using the pressure regulators and control valves. During a cold flow the approximate mass flow and the propellants mixture ratio was checked and corrected if not in the desired range. Subsequent to the cold flows, the test sequence was started. The setup was purged with nitrogen for 3 s, followed by 10 s of waiting to release the nitrogen pressure. Then the spark plug was activated and shortly afterwards the N_2O and C_2H_4 valves were opened. During all tests the burn time was

set to 10 s to assure a steady state combustion and a sufficient time span to evaluate the chamber pressure and the mass flow.

The hot run ended with closing the N_2O and C_2H_4 valves. After the test run all valves were kept closed for 35 s to allow an equalization of the temperature in the chamber. For the later heat flux calculation the average chamber temperature 30 s after closing the feeding valves was taken into account. Subsequent to this waiting time, the whole setup was purged with nitrogen again. Each test was repeated twice with nearly identical mass flow and mixture ratio, slight variations in the mixture ratio and mass flow were caused by small differences of the supply pressure in between two test runs.

4. Theoretical Performance Calculation, c^*_{theo}, I_{sp} and Combustion Temperature T_c

In a first step the theoretic performance of the propellant mixture was assessed by means of NASA CEA.[16]

Figure 4 shows the theoretical specific Impulse I_{sp}, the theoretical, characteristic exhaust velocity c^*_{theo} and combustion temperature T_c depending on the mixture ratio (ROF). For calculating the I_{sp} expansion in vacuum and an expansion ratio ϵ of 50 was chosen. All calculations were performed assuming frozen reactions at the nozzle throat. Furthermore the I_{sp}, c^*_{theo} and T_c were calculated for a chamber pressure of 5 and 10 bar, while the unburned gas temperature was 283 K.

(a) Specific impulse I_{sp} and combustion Temperature T_c depending on mixture ROF

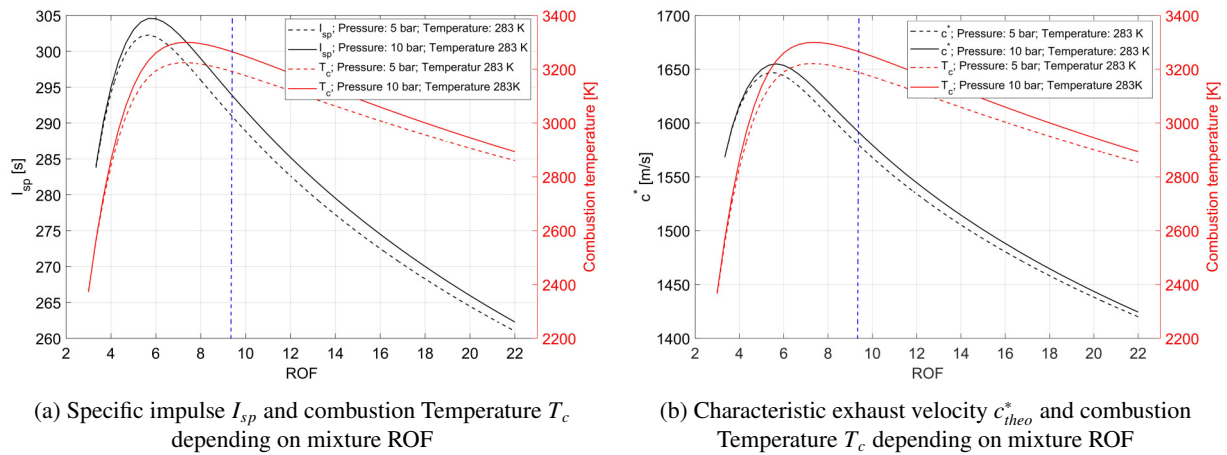(b) Characteristic exhaust velocity c^*_{theo} and combustion Temperature T_c depending on mixture ROF

Figure 4: Specific impulse I_{sp}, characteristic exhaust velocity c^*_{theo} and combustion temperature T_c depending on mixture ratio. Calculation with NASA CEA,[16] frozen at throat and expansion ratio ϵ=50

The solid lines in figure 4a and figure 4b give I_{sp}, c^*_{theo} and T_c for 10 bar chamber pressure and 283 K propellant inlet temperature. The dashed lines mark the values for 5 bar chamber pressure and 283 K.

Figure 4a shows a maximum I_{sp} of 305 s at a mixture ratio in between 5.5 and 6 at 10 bar chamber pressure. The maximum combustion temperature of 3300 K for 10 bar chamber pressure is reached at a mixture ratio of 7.3. The blue dashed line symbolizes the stoichiometric mixture ratio which is 9.41. Figure 4b gives the theoretical c^*_{theo} again in comparison to the combustion temperature T_c. At a mixture ratio of 5.7 a maximum c^*_{theo} of 1655 m/s is reached for a chamber pressure of 10 bar and a propellant inlet temperature of 283 K.

5. Test Results and Discussion

In this section the results of four different test campaigns with more than 60 single test runs are evaluated. For each test run, the average pressure in the combustion chamber, the mean mass flow for the given test run and the measured nozzle throat diameter were taken into account. To assure a steady state combustion and to wait for the rise time of the Coriolis mass flow sensors, the evaluation slot for averaging the pressure and mass flow was in between second four and second ten.

First the experimentally derived c^*_{exp} and η_{c^*} depending on the mixture ratio will be shown and discussed. Second the measured and calculated heat flux depending on the mixture ratio will be analysed and compared to the results of the above mentioned Nusselt correlations.

Furthermore for a variation of the chamber pressure p_c, the chamber length (l_{seg} or L^*) and the mass flux j_m, the experimentally observed combustion efficiency η_{c^*} and heat flux will be shown and discussed. In a final step, a modification to the Nusselt equations is shown, which describes the observed heat fluxes with greater accuracy.

ANALYSIS OF COMBUSTION EFFICIENCY AND HEAT LOADS AN A N_2O/C_2H_4 COMBUSTOR

5.1 c^*_{exp}, η_{c^*} and Heat Flux Depending on Mixture Ratio (ROF)

Figure 5 gives the characteristic exhaust velocity c^*_{exp} as determined during the experiments. The calculation of c^*_{exp} was done according to equation (1). Table 1 summarizes the boundary conditions for this test campaign. While the chamber segment length l_{seg}, the nozzle throat diameter, the chamber pressure and the test duration were kept constant, the mixture ratio was varied in between 3.4 and 22. The stoichiometric propellant mixture has an O/F of 9.41.

Table 1: Operating points of the combustion chamber to analyse the influence of the mixture ratio ROF

$l_{seg}[mm]$	$d_{th}[mm]$	$p_c[bar]$	$ROF[-]$	test duration $[s]$	$L^*[m]$
20	5	7.5	**3.4-22**	10	1.02

Figure 5a shows the experimental c^*_{exp} and the corresponding theoretical c^*_{theo} depending on the mixture ratio. For this test series a maximum c^*_{exp} of 1530 m/s at a mixture ratio of 6.8 was observed. When moving to richer or leaner mixtures, the experimental and theoretical c^* drops, while for a propellant with a mixture ratio richer than 3.38 most of the test resulted in a flame out.
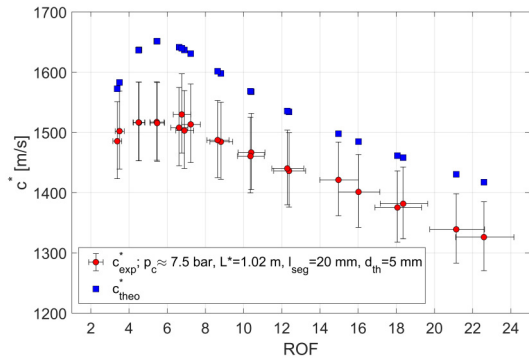
(a) Experimental and theoretical c^* depending on mass mixture ratio ROF for fixed pressure, chamber length and nozzle diameter
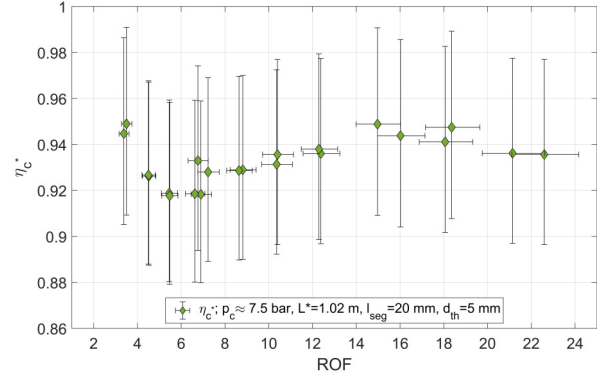
(b) combustion efficiency η^*_c depending on mass mixture ratio ROF for fixed pressure, chamber length and nozzle diameter

Figure 5: Experimental and theoretical c^* and η_{c^*} depending on mixture ratio ROF for tests with an average pressure of 7.5 bar, an L^* of 1.02 m, chamber segment length of 20 mm and a nozzle throat diameter of 5 mm

The combustion efficiency η^*_c in figure 5b changes slightly with variations in the mixture ratio. This variation is most likely caused by changes in the combustion temperature depending on the current mixture ratio. A higher combustion temperature results in higher heat losses to the chamber walls, thus for mixture ratios with a higher combustion temperature the c^* efficiency is lower. The lowest combustion efficiency of 91.8 % is observed at a mixture ratio of 5.5, here figure 5a shows the largest difference in between the experimental and theoretical c^*.

Figure 6 shows heat flux observed during the experiments and compares it to the Nusselt correlations of Gnielinski, Bartz, Cinjarew and Dittus-Boelter. The experimental heat flux was calculated according to equation (9) by assuming that the heat flux is only applied to the cylindrical part of the combustion chamber. For calculation of the Nusselt numbers according to Gnielinski, Cinjarew and Dittus-Boelter, the fluid properties at the combustion temperature T_c were taken into account. For calculation of the Nusselt number with Bartz' equation the fluid properties at the stagnation temperature T_{stag} (see equation (16)) were used. Taking this reference temperatures into account resulted in the least differences to the experimental data, while other reference temperatures resulted in much bigger differences (up to 100%) between the measured and calculated data.

As figure 6 indicates, depending on the used correlation, difference of up to 0.7 MW/m^2 or 50% in between the measured and calculated heat fluxes are observed. The correlation of Bartz (green line) gives the largest heat fluxes across the whole range of mixture ratios. Despite this general overestimation Bartz' equation predicts the heat flux for rich or lean mixtures (ROF ≤ 5 and ≥ 13) in quite good accordance. The Dittus-Boelter equation (yellow line) results in lower heat fluxes compared to the experimental values, while the correlations proposed by Cinjarew and Gnielinski show a good agreement for near stoichiometric and rich conditions (ROF ≥ 5 and ≤ 11). Despite the differences, the curve of the measured and calculated heat fluxes show a similar shape. In general the peaks of the measured heat flux
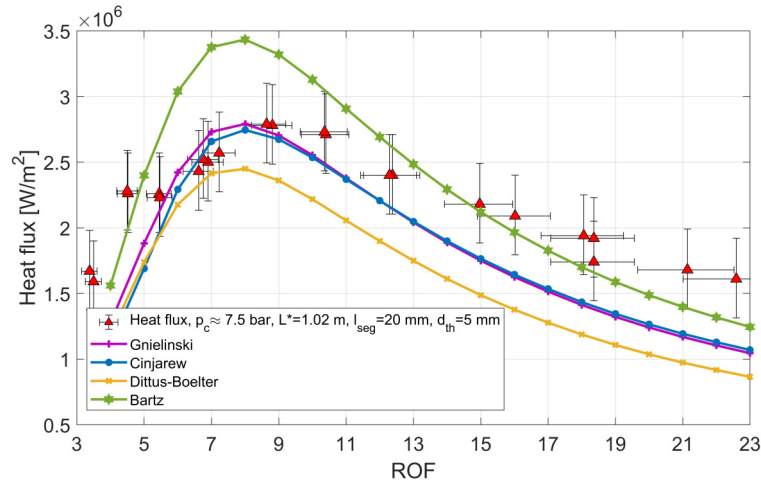
Figure 6: Experimental heat flux and heat flux calculated via Nusselt correlations

near the stoichiometric mixture ratio are lower than the calculated values, while for lean and rich mixture ratios the experimental heat fluxes are higher than the calculated values. For lean (ROF $\leq$ 5) and rich (ROF $\geq$ 13) mixtures the correlation of Bartz seems to provide good results, while for near stoichimetric mixture ratios (ROF $\geq$ 5 and $\leq$ 11) the Cinjarew and Gnielinski correlation give a good estimation of the heat flux.

5.2 η_{c^*} and Heat Flux Depending on Chamber Pressure

In a second test series, the chamber pressure was varied via adjustment of the mass flow, while the mixture ratio, the chamber segment length and nozzle diameter were kept constant. Table 2 shows the boundary conditions for this test series.

Table 2: Operating points of the combustion chamber to analyse the influence of the chamber pressure p_c

$l_{seg}[mm]$	$d_{th}[mm]$	$p_c[bar]$	$ROF[-]$	test duration $[s]$	$L^*[m]$
20	5	**2.7-11.1**	7.1	10	1.02

Figure 7 presents the combustion efficiency η_{c^*} depending on the chamber pressure. With rising chamber pressure, the efficiency also rises. In general the theoretical c^*_{theo} increases with rising chamber pressure due to higher combustion temperatures (see figure 4). However, a rise in theoretical c^* does not directly cause η_{c^*} or c^*_{exp} to rise. Additional effects seem to increase the experimental c^*_{exp} compared to the theoretical values. As it will be shown in section 5.4 an increase in pressure and thus density results in a lower heat loss per mass flow. With increasing pressure the additional energy release caused by the reaction overcompensates the effect of larger heat losses generated by a larger pressure. Finally this results in a higher efficiency at larger chamber pressures.

Figure 7b shows the calculated and measured heat fluxes for different chamber pressures at a mixture ratio of 7.1. The course of the heat flux rise is described in good accordance by most of the correlations, except for the Gnielinski correlation, which gives higher heat fluxes for low chamber pressures and slightly lower heat fluxes for high chamber pressures. The best agreement with the experimental heat flux data is shown by the Cinjarew equation. This is most likely caused by the already good agreement of the Cinjarew equation at near stoichiometric conditions (see figure 6) and a good representation of the heat flux rise with increasing chamber pressure. Fitting of the experimental heat flux data shows a correlation of the heat flux to the chamber pressure with the power of 0.827:

$$\dot{q} \sim p^{0.827} \tag{23}$$

This correlates well to literature data[23] and the above described Nusselt correlations. As the Reynolds number is proportional to the density and the density of an ideal gas proportional to the pressure, the pressure directly influences the Reynolds number. Regarding the Nusselt correlations of Bartz, Dittus-Boelter and Gnielinski the Reynolds number influences the Nusselt number with the power of 0.8, while Cinjarew gives an exponent of 0.82.

ANALYSIS OF COMBUSTION EFFICIENCY AND HEAT LOADS AN A N_2O/C_2H_4 COMBUSTOR
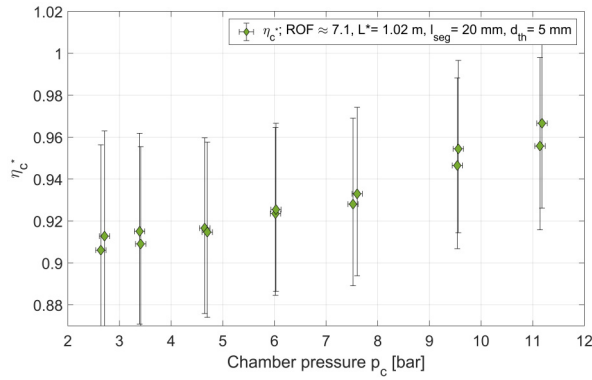
(a) combustion efficiency η_c^* depending on chamber pressure, for fixed mixture ratio, chamber length and nozzle diameter
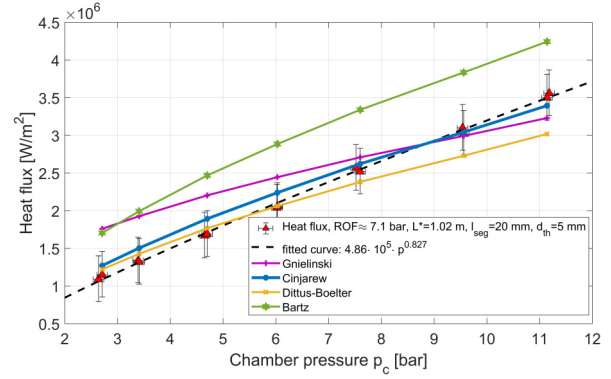
(b) Experimental heat flux depending on chamber pressure and heat flux calculated by Nusselt correlations for fixed mixture ratio, chamber length and nozzle diameter

Figure 7: η_{c^*}, experimental heat flux and heat flux derived by Nusselt correlations depending on chamber pressure for tests with an average mixture ratio of 7.1, an L^* of 1.02 m, chamber segment length of 20 mm and a nozzle throat diameter of 5 mm
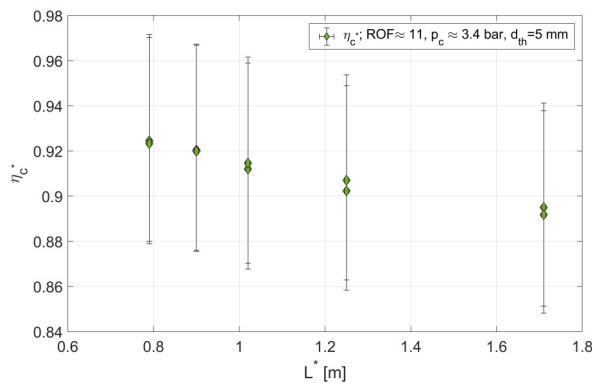
5.3 η_{c^*} and Heat Flux Depending on Chamber Segment Length l_{seg} or Characteristic Chamber Length L^*

A third test series was conducted to evaluate the influence of an increasing chamber length l_{seg} or an increasing surface area A_{cc} on the combustion efficiency and heat loads. With increasing chamber length l_{seg}, the residence time of the flow in the chamber increases and L^* increases for a constant nozzle throat diameter. Table 3 gives the operation points for the test series with variation of the chamber length.

Table 3: Operating points of the combustion chamber to analyse the influence of the characteristic chamber length L^*

$l_{seg}[mm]$	$d_{th}[mm]$	$p_c[bar]$	$ROF[-]$	test duration $[s]$	$L^*[m]$
10 - 50	5	3.4	11	10	**0.79 - 1.71**

As already shown by a previous study[37] the optimum characteristic chamber length L^* for the premixed, gaseous propellant is around 0.5 m. During the current test campaign the trend of decreasing performance with rising chamber length was confirmed. Additionally in the current test campaign the occurring heat loads were derived. Figure 8a shows the combustion efficiency depending on the characteristic chamber length L^*. As during this test campaign only the chamber segment length l_{seg} and not the nozzle throat diameter was varied, the changes in L^* directly correspond to the changes in the chamber length (see equation (4)).

(a) combustion efficiency η_c^* depending on chamber length for fixed mixture ratio, chamber pressure and nozzle diameter
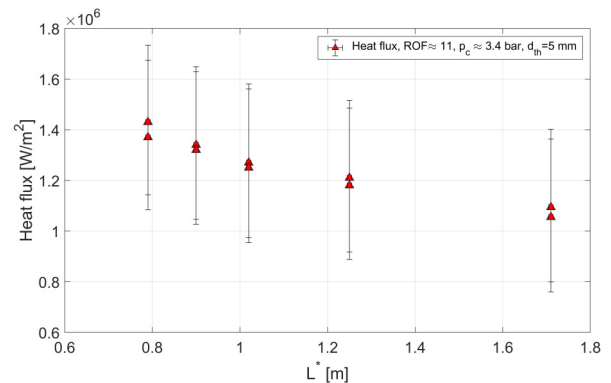
(b) Heat flux depending on chamber length for fixed mixture ratio, chamber pressure and nozzle diameter

Figure 8: η_{c^*} and heat flux depending on chamber length for tests with an average mixture ratio of 11, an average chamber pressure 3.4 bar and a nozzle throat diameter of 5 mm

As shown in figure 8a the c^* efficiency drops from 92.5% to 89.5% when L^* is increased from 0.79 m to 1.71 m. The increase in surface area of the combustion chamber causes a larger heat flow $\dot{Q}$ to be lost to the chamber walls. While figure 8b shows a decrease of the heat flux $\dot{q}$ with increasing chamber length and increasing chamber surface area, the overall heat flow $\dot{Q}$ increases with rising chamber length. If e.g. the characteristic chamber length and thus the chamber surface area doubles from 0.8 m to 1.6, the heat flux only drops from approximately 1.4 to 1.1 MW/m^2. Extrapolated to the heat flow $\dot{Q}$ a doubled surface area and a 22% decrease in heat flux results in a 1.56 times higher heat flow. Due to this increase in overall heat flow $\dot{Q}$, the combustion efficiency drops with increasing chamber length. Furthermore the drop of the heat flux with increasing chamber length also indicates that the maximum heat flux to the chamber walls will be located near to the injector at an L^* smaller 0.79 m.

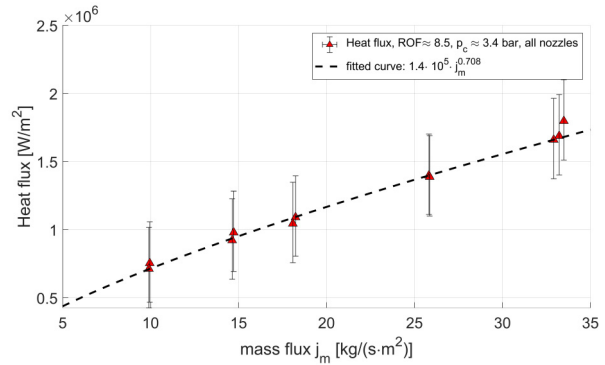### 5.4 η_{c^*} and Heat Flux Depending on Mass Flux j_m

A fourth test series was conducted to evaluate the influence of the mass flux on the combustion efficiency and the heat flux. The boundary conditions for this test series are given in table 4, while the nozzle throat diameter and with this the L^* was changed, the chamber surface area and chamber segment length was kept constant. Furthermore the mixture ratio and the chamber pressure were fixed to a very narrow range to evaluate the influence of the mass flux only.

Table 4: Operating points of the combustion chamber to analyze the influence of the mass flux

$l_{seg}[mm]$	$d_{th}[mm]$	$p_c[bar]$	$ROF[-]$	test duration $[s]$	$L^*[m]$
20	**5 - 9**	3.4	11	10	**0.26 - 0.79**
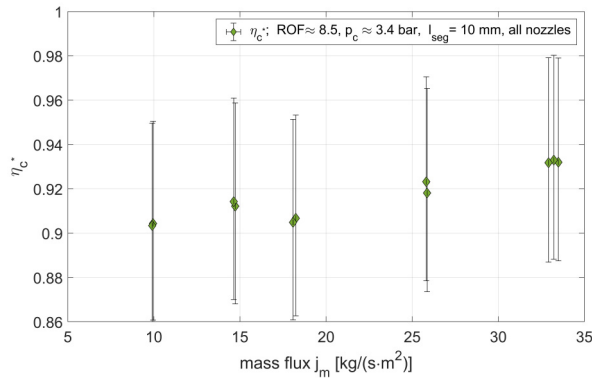
(a) Combustion efficiency η_{c^*} depending on mass flux for fixed mixture ratio, chamber pressure, chamber segment length and nozzle diameters in between 5 and 9 mm

(b) Heat flux depending on mass flux for fixed mixture ratio, chamber pressure, chamber segment length and nozzle diameters in between 5 and 9 mm

Figure 9: η_{c^*} and heat flux depending on mass flux for tests with an average mixture ratio of 8.5, an average chamber pressure 3.4 bar, a chamber segment length of 10 mm and nozzle throat diameters ranging from 5 mm - 9 mm

Figure 9a gives the combustion efficiency depending on the mass flux j_m. A moderate increase of the efficiency from 90.5% at a mass flux of 10 $kg/(s \cdot m^2)$ to an efficiency of 93% at a mass flux of 33 $kg/(s \cdot m^2)$ can be observed. As figure 9b shows, the heat flux also rises with increasing mass flux. Fitting of the experimental data shows a proportionality of the heat flux to the mass flux to the power of 0.702:

$$\dot{q} \sim j_m^{0.702} \tag{24}$$

As the mass flux j_m is:

$$j_m = \frac{\dot{m}}{A_{cc}} = \frac{\rho \cdot v \cdot A_{cc}}{A_{cc}} = \rho \cdot v \tag{25}$$

and the pressure and thus the density was kept constant during this test series, the increase in heat flux with increasing mass flux is presumably caused by the increase of the flow velocity v:

$$\dot{q} \sim v^{0.702} \tag{26}$$

ANALYSIS OF COMBUSTION EFFICIENCY AND HEAT LOADS AN A N_2O/C_2H_4 COMBUSTOR

If during the test series the mixture ratio and the chamber pressure are kept constant, the average flow velocity in the combustion chamber increases with rising nozzle throat area, respectively nozzle throat diameter. Higher flow velocities result in higher Reynolds numbers which again increase the heat flux to the chamber walls. Furthermore the flow field in the chamber might change with increasing mass flow, which then changes the heat loads to the chamber walls. Those differences in the flow field could be caused by a change or occurrence of a recirculation zone downstream the injector in the combustion chamber. The recirculation zone might be formed by the rapid change of the diameter and the corresponding expansion, when the flow leaves the injector and enters the chamber (see figure 2).
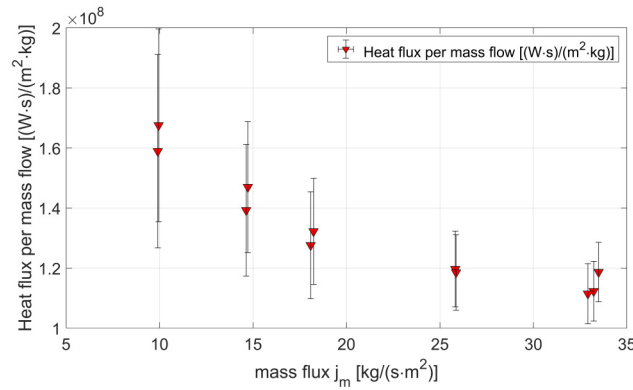

Figure 10: Heat flux per mass flow depending on mass flux

Figure 10 shows the average heat flux per mass flow depending on the mass flux. The diagram indicates that with increasing mass flux, respectively velocity, the heat loss per mass drops as the density is constant in this test series. This effect explains the rising combustion efficiency with increasing mass flux. As the heat loss per mass element decreases with increasing mass flux, a smaller percentage of the energy is lost to the chamber walls with increasing mass flux. As a consequence η_{c^*} rises.

5.5 Modification of the Nusselt Correlations to Improve the Heat Flux Prediction

Due to the big differences of the calculated values for reach or lean mixtures, a modification of the Nusselt correlations was employed. To improve the accuracy of the mentioned correlations, the correction factor ζ was introduced:

$$\zeta = 1 + 0.163 \cdot \left(\frac{ROF}{ROF_{st}} - 1 \right)^2 \tag{27}$$
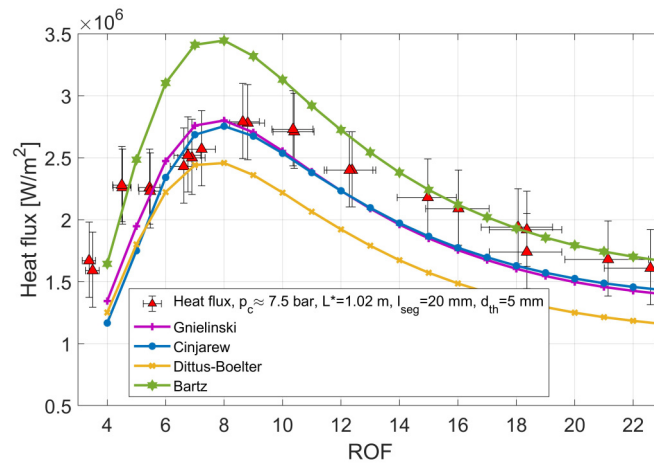

Figure 11: Experimental heat flux and heat flux calculated via modified Nusselt correlations

Here ROF_{st} indicates the mixture ratio at stoichiometric conditions, which is 9.41 for the N_2O/C_2H_4 mixture. By using the correction factor, the Nusselt number is modified according to equation (28):

$$Nu_{mod} = Nu \cdot \zeta \tag{28}$$

Figure 11 shows the results for the heat flux calculated with the four modified Nusselt correlation (28). For stoichiometric conditions, the heat flux stays at the same level, while for rich and lean conditions the prediction is improved slightly (compare figure 6 and figure 11). Nevertheless, no single correlation can predict the measured heat fluxes across the whole range of mixture ratios.

As mentioned before, Bartz' equation gives a good prediction for the rich (ROF $\leq$ 5) and lean (ROF $\geq$ 13) mixture ratios, while the heat loads at near stoichiometric mixture ratios (ROF $\geq$ 5 and $\leq$11) are well predicted by Cinjarew's and Gnielinski's equation.

5.6 Error Analysis

To analyze the possible errors, the pressure and temperature sensors were compared to a calibrated device (Beamex MC 5, Modul EXT 250 and Beamex FB660 Field Temperature Block). The comparison resulted in a maximum deviation of 3 K or 4% for the thermocouples over a temperature range up to 600°C, while the largest error of the pressure sensors' was 0.1 bar or 0.8% in between 1 and 40 bar. Due to a high contraction ratio of the combustion chamber even for the largest nozzle throat, low Mach numbers in the chamber occurred. Thus for the calculation of the c^* values a correction of the experimental pressure data to obtain the stagnation or total pressure was not employed.

The two Coriolis mass flow meter (Rheonik RHM 015 and RHM 04) were compared to a third just calibrated reference mass flow meter. Despite the manufacturers specification, differences of up to 5% in between the reference mass flow meter and the two other Coriolis sensors were observed.

The nozzle throat diameter was measured via micrometer, here a measurement accuracy of 2% on the throat area was assumed.

For calculation of the c^* the average mass flow and pressure in between 4 and 10 s of each test run was taken into account. To determine the heat flux $\dot{q}$ an error of the heat capacity c_p of 50 $J/(kg \cdot K)$ was assumed, while the error on the test duration Δt was estimated to be 0.2 s due to the transient ignition process. The temperature error to calculate the heat flux was estimated to be within 5 K due to small temperature differences in the whole chamber 30 s after shutdown, due to heat conduction to the feeding lines and due to heat losses to the surrounding atmosphere. The mass of the chamber segments was determined by a calibrated scale so this error was assumed to be small and was thus neglected.

The error bars were calculated using a worst case approach. For example the maximum error of the c^* value according to equation (1) is determined using the maximum possible occurring pressure, the maximum nozzle area and the minimal mass flow. Therefore Δc^*_{max} is calculated as shown in equation (29). Errors of other variables were calculated the same way.

$$\Delta c^*_{max} = \frac{(p_c + \Delta p_c)(A_{th} + \Delta A_{th})}{\dot{m} + \Delta \dot{m}} - c^*_{exp} \tag{29}$$

6. Summary

In sum four test series with a premixed, gaseous green propellant consisting of N₂O and C₂H₄ were conducted. The aim of the test campaign was to evaluate the influence of the mixture ratio ROF, the chamber pressure p_c, the chamber length L^* and the muss flux j_m on the characteristic exhaust velocity c^*, on the combustion efficiency η_{c^*} and on the heat flux $\dot{q}$ to the chamber walls. To perform the experiments a CuCr1Zr rocket combustion chamber equipped with several temperature and pressure sensors was used. The chamber was not equipped with an active cooling system, thus the combustion process resulted in heating of the chamber segments.

In a first step the theoretical values for c^*, I_{sp} and the combustion temperature T_c were calculated via NASA CEA.[16] Second the theoretical c^*_{theo} was calculated for each test point of the combustion tests. By dividing the experimental c^*_{exp} by the theoretical c^*_{theo} the combustion efficiency η_{c^*} for all test series was derived. Furthermore by taking the temperature rise in the chamber segments ΔT, the heat capacity c_p, the mass of the chamber segments m_{seg}, the chamber surface area A_{seg} and the test duration Δt into account, the average heat flux $\dot{q}$ to the combustion chamber was determined. The heat flux was additionally compared to the predictions of four empirical Nusselt correlations. Here the Nusselt correlations of Bartz, Cinjarew, Dittus-Boelter and Gnielinski were used to calculate the hot gas side heat transfer.

Regarding the four different test series, the following observations were made:

a) Due to large changes in the combustion temperature c^* changes significantly with the mixture ratio ROF. Additionally the combustion efficiency η_{c^*} is effected by the mixture ratio, because the respective combustion temperature results in higher or lower heat losses to the chamber walls. Higher combustion temperatures and thus higher losses to the chamber walls result in lower c^* efficiency, e.g. for near stoichiometric conditions the heat losses are at a maximum.

b) The combustion efficiency rises with increasing chamber pressure. For higher chamber pressures the energy generation by the combustion process overcompensates the heat losses to the chamber walls, thus the efficiency rises. For the used combustor the heat losses to the chamber walls are proportional to the chamber pressure to the power of 0.827:

$$\dot{q} \sim p_c^{0.827} \tag{30}$$

This e.g. means a doubling of the mass flow results in a doubling of the chamber pressure, while the heat flux just grows by a factor of 1.77. Additionally the theoretical c_{theo}^* also rises due to higher combustion temperatures with higher chamber pressures.

c) The combustion efficiency η_{c^*} and the heat flux $\dot{q}$ per chamber segment decrease with increasing chamber length. Due to the premixed, gaseous state of the propellant, the flame and the combustion zone is located very close to the injector. Thus the maximum heat flux occurs near the injector. If the chamber length and the chamber surface area is increased, the average heat flux per chamber segment decreases due to a declining heat flux downstream of the injector. Despite the heat flux decreases with increasing chamber length, the overall heat losses caused by an increase of chamber surface area surpass the decrease of the heat flux. Thus a larger chamber length reduces the combustion efficiency due to additional heat losses.

d) The combustion efficiency η_{c^*} and the heat flux $\dot{q}$ increase with growing mass flux j_m. For identical pressure and mixture ratio, η_{c^*} slightly increases with higher mass flux, while the heat flux grows to the mass flux or the velocity to the power of 0.702:

$$\dot{q} \sim j_m^{0.702} \sim v^{0.702} \tag{31}$$

A growing mass flux at constant pressure and density results in a growing flow velocity. The larger velocity leads to a higher heat flux, due to a larger Reynolds number as already predicted by the Nusselt correlations. Nevertheless the average heat loss per mass flow declines with increasing mass flux. In sum this results in lower overall heat losses at higher mass fluxes and an increase in η_{c^*}. The changes in the heat loss with variations of the mass flux might also be caused by changes in the flow field inside the combustion chamber. So e.g. occurrence or movement of recirculation zones might influence the overall heat flux.

Finally, to improve the accuracy of the used Nusselt correlations, the calculated Nusselt number was multiplied by the expression ζ:

$$\zeta = 1 + 0.163 \cdot \left(\frac{ROF}{ROF_{st}} - 1 \right)^2 \tag{32}$$

ζ modifies the resulting Nusselt number with respect to changes in the mixture ratio. The modified Nusselt number Nu_{mod} then is given by:

$$Nu_{mod} = Nu \cdot \zeta \tag{33}$$

By using the modified Nusselt number, the prediction of the Bartz correlation for rich and lean mixture ratios (ROF $\leq$ 5 and ROF $\geq$ 13) is improved. For near stoichiometric mixture ratios (ROF $\geq$ 5 and ROF $\leq$ 11) the Cinjarew equation gives a reasonable approximation of the experimental heat flux.

7. Acknowledgments

ANALYSIS OF COMBUSTION EFFICIENCY AND HEAT LOADS AN A N_2O/C_2H_4 COMBUSTOR

Nomenclature

Latin Symbols	Description	Unit
A_{cc}	Combustion chamber cross sectional area	$[m^2]$
A_{ref}	Reference surface area	$[m^2]$
A_{seg}	Inner surface area of chamber segment	$[m^2]$
A_{th}	Nozzle throat area	$[m^2]$
c^*_{exp}	Experimental characteristic exhaust velocity	$[\frac{m}{s}]$
c^*_{theo}	Theoretical characteristic exhaust velocity	$[\frac{m}{s}]$
c_p	Specific heat capacity at constant pressure	$[\frac{J}{kg \cdot K}]$
d	Diameter	$[m]$
d_{th}	Nozzle throat diameter	$[m]$
I_{sp}	Specific impulse	$[s]$
j_m	Mass flux	$[\frac{kg}{s \cdot m^2}]$
l	characteristic length	$[m]$
l_{pipe}	Pipe length	$[m]$
L^*	Characteristic chamber length	$[m]$
L_{cc}	Combustion chamber length	$[m]$
$\dot{m}$	Mass flow	$[\frac{kg}{s}]$
m_{seg}	Mass of chamber segment	$[kg]$
Ma	Mach number	$[-]$
Nu	Nusselt number	$[-]$
Nu_{mod}	Modified Nusselt number	$[-]$
p_c	Combustion chamber pressure	$[bar]$
Pr	Prandtl number	$[-]$
$\dot{q}$	Heat flux	$[\frac{W}{m^2}]$
$\dot{q}_{wall}$	Heat flux to chamber walls	$[\frac{W}{m^2}]$
$\dot{Q}$	Rate of heat flow	$[W]$
Re	Reynolds number	$[-]$
ROF	Ratio oxidizer to fuel O/F	$[-]$
ROF_{st}	Stoichiometric mixture ratio	$[-]$
T_c	Adiabatic combustion temperature	$[K]$
T_{in}	Fluid inlet temperature	$[K]$
T_{mean}	Mean temperature	$[K]$
T_{out}	Fluid outlet temperature	$[K]$
T_{ref}	Reference temperature	$[K]$
T_{stag}	Stagnation or total temperature	$[K]$
T_{stat}	Static temperature	$[K]$
T_{wall}	Wall temperature	$[K]$
v	flow velocity	$[\frac{m}{s}]$

ANALYSIS OF COMBUSTION EFFICIENCY AND HEAT LOADS AN A N_2O/C_2H_4 COMBUSTOR

Greek Symbols	Description	Unit
α	Convective heat transfer coefficient	$[\frac{W}{m^2 \cdot K}]$
Δc^*_{max}	Maximum value for the error of c^*	$[\frac{m}{s}]$
ΔT	Temperature rise in walls	$[K]$
Δt	test duration	$[s]$
ϵ	Expansion ratio: Area of nozzle exit divided by area of nozzle throat	$[-]$
ζ	Modification function to the Nusselt number	$[-]$
η_{c^*}	c^* or combustion efficiency	$[-]$
κ	Heat capacity ratio	$[-]$
λ	Thermal conductivity	$[\frac{W}{m \cdot K}]$
μ	Dynamic viscosity	$[\frac{m^2}{s}]$
ρ	Density	$[\frac{kg}{m^3}]$

References

[1] *VDI heat atlas*. VDI-Buch. Springer-Verlag Berlin Heidelberg, Berlin, 2. ed. edition, 2010.

[2] Rachid Amrousse, Toshiyuki Katsumi, Nobuyuki Azuma, and Keiichi Hori. Hydroxylammonium nitrate (HAN)-based green propellant as alternative energy resource for potential hydrazine substitution: From lab scale to pilot plant scale-up. *Combustion and Flame*, 176(1):334–348, 2017.

[3] Kjell Anflo and Crowe B. Two years of in-space demonstration and qualification of an ADN-based propulsion system on PRISMA. In *47th AIAA/ASME/SAE/ASEE Joint Propulsion Conference, 31. July-03 August 2011, San Diego, California, USA*.

[4] Kjell Anflo and R. Möllerberg. Flight demonstration of new thruster and green propellant technology on the PRISMA satellite. *Acta Astronautica*, 65(9-10):1238–1249, 2009.

[5] Kjell Anflo, R. Mollerberg, and Neff, K. and King, Paul. High Performance Green Propellant for Satellite Applications. In *45th AIAA/ASME/SAE/ASEE Joint Propulsion Conference & Exhibit*, 02 August 2009 - 05 August 2009.

[6] Hans Dieter Baehr and Karl Stephan. *Heat and Mass Transfer*. Springer-Verlag Berlin Heidelberg, Berlin, Heidelberg, 3., rev. ed. edition, 2011.

[7] D. R. Bartz. A Simple Equation for Rapid Estimation of Rocket Nozzle Convective Heat Transfer Coefficients: Technical Notes. *Journal of Jet Propulsion*, 27(1):49–53, 1957.

[8] D. R. Bartz. Survey of the relationship between theory and experiment for convective heat transfer from rocket combustion gases. *Agard Advan. in tactical rocket propulsion*, 1968:291–381, 1968.

[9] Ognjan Božić, Dennis Porrmann, Daniel Lancelle, and Stefan May. Enhanced development of a catalyst chamber for the decomposition of up to 1.0 kg/s hydrogen peroxide. *CEAS Space Journal*, 8(2):77–88, 2016.

[10] Robert Bruce, Gary Taylor, Robert Ross, and Don Beckmeyer. Propulsion Ground Testing with High Test Peroxide-Lessons Learned. In *22nd AIAA Aerodynamic Measurement Technology and Ground Testing Conference*, Reston, Virigina, 2002. American Institute of Aeronautics and Astronautics.

[11] Helmut K. Ciezki, Lukas Werling, Michele Negri, Friedolin Strauss, Mario Kobald, Christoph Kirchberger, Dominic Freudenmann, Marius Wilhelm, and Anna Petrarolo. 50 Years of Test Complex M11 in Lampoldshausen - Research on Space Propulsion Systems for Tomorrow. In *7th European Conference for Aeronautics and Space Sciences (EUCASS), 03. - 06. Jul. 2017, Milano, Italy*. 2017.

[12] Peter Friedhoff, Alisa Hawkins, John Carrico, Jonathan Dyer, and Kjell Anflo. In-Orbit Operation and Performance of Ammonium Dinitramide (ADN) Based High Performance Green Propulsion (HPGP) Systems. In *53rd AIAA/SAE/ASEE Joint Propulsion Conference, AIAA Propulsion and Energy Forum*. 2017.

[13] A. Fröhlich, M. Popp, G. Schmidt, and D. Thelemann. Heat transfer characteristics of H2/O2-combustion chambers. In *29th Joint Propulsion Conference and Exhibit 28. June - 30. June 1993. Monterey, CA, USA*.

[14] Volker Gnielinski. Neue Gleichungen für den Wärme- und den Stoffübergang in turbulent durchströmten Rohren und Kanälen. *Forschung im Ingenieurwesen A*, 41(1):8–16, 1975.

[15] Amir S. Gohardani, Johann Stanojev, Alain Demairé, Kjell Anflo, Mathias Persson, Niklas Wingborg, and Christer Nilsson. Green space propulsion: Opportunities and prospects. *Progress in Aerospace Sciences*, 71(1):128–149, 2014.

[16] Sanford Gordon and Bonnie McBride. Computer Program for Calculation of Complex Chemical Equilibrium Compositions and Applications: NASA Reference Publication 1311: I. Analysis, 1996.

[17] Ulrich Gotzig. Challenges and Economic Benefits of Green Propellants for Satellite Propulsion: 9 pages. In *7th European Conference for Aeronautics and Space Sciences (EUCASS), 03. - 06. Jul. 2017, Milano, Italy*. 2017.

[18] Ulrich Gotzig, Stephan Kraus, Dietmar Welberg, Daniel Fiot, Pierre Michaud, Christian Desaguier, Santiago Casu, Bastian Geiger, and Rainer Kiemel. Development and Test of a 3D printed Hydrogen Peroxide Flight Control Thruster. In *51st AIAA/SAE/ASEE Joint Propulsion Conference, 27.-29. July 2015, Orlando, Florida, USA*, 2015.

[19] Ben Greene, David L. Baker, and Wayne Frazier. Hydrogen Peroxide Accidents and Incidents: What We Can Learn From History. In *32nd PDCS Joint JANNAF Meeting; 26-30 Jul. 2004*.

[20] Nicholas-Etienne Harmansa, Georg Herdrich, and Stefanos Fasoulas. Development of a Water Propulsion System for Small Satellites. In *68th International Astronautical Congress 25.-29.09.2017*.

[21] Nicholas-Etienne Harmansa, Georg Herdrich, Stefanos Fasoulas, and Ulrich Gotzig. Development of a water electrolysis propulsion system for small satellites. In *Space Propulsion Conference 14.-18.05.2018, Sevilla, Spain*.

[22] Keiichi Hori. Lessons Learned in the Thruster Tests of HAN. In *Chemical Rocket Propulsion*, Springer Aerospace Technology, pages 801–818. Springer International Publishing, Cham and s.l., 2017.

[23] D. Huzel and D. Huang. *Modern Engineering for Design of Liquid-Propellant Rocket Engines*. American Institute of Aeronautics & Astronautics, Inc, Washington.

[24] Frank P. Incropera, David P. DeWitt, Theodore L. Bergman, and Adrienne S. Lavine. *Fundamentals of heat and mass transfer*. Wiley, Hoboken, NJ, 6. ed. edition, 2007.

[25] Christoph Kirchberger. *Investigation on heat transfer in small hydrocarbon rocket combustion chambers: Zugl.: München, Techn. Univ., Diss., 2014*. Raumfahrt. Verl. Dr. Hut, München, 1. aufl. edition, 2014.

[26] Christoph Kirchberger, Andreas Hupfer, Hans-Peter Kau, Sebastian Soller, Philip Martin, Marc Bouchez, and Emmanuel Dufour. Improved Prediction of Heat Transfer in a Rocket Combustor for GOX/Kerosene. In *47th AIAA Aerospace Sciences Meeting including The New Horizons Forum and Aerospace Exposition*, 05 January 2009 - 08 January 2009.

[27] Felix Lauck, Michele Negri, Marius Wilhelm, Dominic Freudenmann, Stefan Schlechtriem, Malte Wurdak, and Ulrich Gotzig. Test bench preparation and hot firing tests of a 1N hydrogen peroxide monpropellant thruster. In *Space Propulsion Conference 14.-18.05.2018, Sevilla, Spain*.

[28] Robert Masse, May Allen, Ronald Spores, and Elizabeth A. Driscoll. AF-M315E Propulsion System Advances and Improvements. In *52nd AIAA/SAE/ASME Joint Propulsion Conference, 25.-27. July 2017, Salt Lake City, Utah, USA*. 2017.

[29] Alfons E.H.J. Mayer, W.P.W. Wieling, A. Watts, M. Poucet, Ian Waugh, J. Macfarlane, and Ferran Valencia-Bel. European Fuel Blend development for in-space propulsion. In *Space Propulsion Conference 14.-18.05.2018, Sevilla, Spain*.

[30] Greg Mungas. NOFBX™ Propulsion Overview: Propulsion Challenges for Commercial Reusable Space Vehicles. In *49th AIAA/ASME/SAE/ASEE Joint Propulsion Conference, 15. - 17. July, 2013, San Jose, California, USA*, Reston, Virginia, 2013. American Institute of Aeronautics and Astronautics.

[31] Michele Negri, Marius Wilhelm, Christian Hendrich, Niklas Wingborg, Linus Gediminas, Leif Adelöw, Corentin Maleix, Pierre Chabernaud, Rachid Brahmi, Romain Beauchet, Yann Batonneau, Charles Kappenstein, Robert-Jan Koopmans, Sebastian Schuh, Tobias Bartok, Carsten Scharlemann, Ulrich Gotzig, and Martin Schwentenwein. New technologies for ammonium dinitramide based monopropellant thrusters – The project RHEFORM. *Acta Astronautica*, 143(1):105–117, 2018.

[32] Nikolaos Perakis, Lukas Werling, Helmut Ciezki, and Stefan Schlechtriem. Numerical Calculation of Heat Flux Profiles in a N2O/C2H4 Premixed Green Propellant Combustor using an Inverse Heat Conduction Method. In *Space Propulsion Conference, 1.-5. May 2016, Rome, Italy*.

[33] Mathias Persson, Kjell Anflo, Aaron Dinardi, and J. Bahu. A Family of Thrusters for ADN-Based Monopropellant LMP-103S. In *48th AIAA/ASME/SAE/ASEE Joint Propulsion Conference & Exhibit*.

[34] Robert L. Sackheim and Robert K. Masse. Green Propulsion Advancement: Challenging the Maturity of Monopropellant Hydrazine. *Journal of Propulsion and Power*, 30(2):265–276, 2014.

[35] Ronald A. Spores. GPIM AF-M315E Propulsion System. In *51st AIAA/SAE/ASEE Joint Propulsion Conference, 27.-29. July 2015, Orlando, Florida, USA*, 2015.

[36] George P. Sutton, Oscar Biblarz, and George Paul Sutton. *Rocket propulsion elements*. John Wiley & Sons and Wiley, Hoboken, N.J, 8th ed. edition, 2010.

[37] Lukas Werling, Patrick Bätz, Helmut Ciezki, and Stefan Schlechtriem. Influence of combustion chamber size (L*) on characteristic exhaust velocity (c*) for a N2O/C2H4 premixed green propellant. In *Space Propulsion Conference 14.-18.05.2018, Sevilla, Spain*.

[38] Lukas Werling, Matthias Hassler, Felix Lauck, Helmut K. Ciezki, and Stefan Schlechtriem. Experimental Performance Analysis (c* & c* Efficiency) of a Premixed Green Propellant consisting of N2O and C2H4. In *53rd AIAA/SAE/ASEE Joint Propulsion Conference, 10-12 July 2017, Atlanta, GA, USA*. 2017.

[39] Lukas Werling, Yannick Jooß, Maximilian Wenzel, Helmut K. Ciezki, and Stefan Schlechtriem. A premixed green propellant consisting of N_2O and C_2H_4: Experimental analysis of quenching diameters to desing flashback arresters. *International Journal of Energetic Materials and Chemical Propulsion*, 17(3):241–262, 2018.

[40] Lukas Werling, Felix Lauck, Dominic Freudenmann, Nicole Röcke, Helmut Ciezki, and Stefan Schlechtriem. Experimental Investigation of the Flame Propagation and Flashback Behavior of a Green Propellant Consisting of N2O and C2H4. *Journal of Energy and Power Engineering*, 11(12):735–752, 2017.

[41] Lukas Werling, Nikolaos Perakis, Steffen Müller, Andreas Hauk, Helmut Ciezki, and Stefan Schlechtriem. Hot firing of a N2O/C2H4 premixed green propellant: First combustion tests and results. In *Space Propulsion Conference, 1.-5. May 2016, Rome, Italy*.

[42] Marius Wilhelm, Christian Hendrich, Herbert Zimmermann, Helmut Ciezki, and Stefan Schlechtriem. Test Facility for Research on Advanced Green Propellants under High-Altitude Conditions. In *Space Propulsion Conference 14.-18.05.2018, Sevilla, Spain*.

[43] Marius Wilhelm, Michele Negri, Christian Hendrich, Niklas Wingborg, Linus Gediminas, Leif Adelö, Corentin Maleix, Pierre Chabernaud, Rachid Brahmi, Romain Beauchet, Yann X. Batonneau, Charles Kappenstein, Robert-Jan Koopmans, Sebastian Schuh, Tobias Bartok, Carsten A. Scharlemann, Kjell Anflo, Mathias Persson, Wilhelm Dingertz, and Ulrich Gotzig. The RHEFORM Project - Developments for ADN-Based Liquid Monopropellant Thrusters. In *53rd AIAA/SAE/ASEE Joint Propulsion Conference, 10-12 July 2017, Atlanta, GA, USA*. 2017.